# Tuning the Doping of Europium in Gadolinium Borate Microparticles at Mesoscale Toward Efficient Production of Red Phosphors

Simin Cui,[†,‡] Xianglei He,[†,‡] Dan Wang,*[,†] Jie-Xin Wang,[†,‡] Yuan Pu,*[,‡] and Jian-Feng Chen[†,‡]

[†]State Key Laboratory of Organic-Inorganic Composites and [‡]Research Center of the Ministry of Education for High Gravity Engineering and Technology, Beijing University of Chemical Technology, Beijing 100029, China

Ⓢ Supporting Information

ABSTRACT: The ideal product of rare-earth-doped phosphors should have uniform particle size distribution and homogeneous doping ions in each particle, and therefore, intensified micromixing at mesoscale is highly required. In this article, inspired by the concept of "mesoscience", we demonstrate the tuning of Eu^{3+} doping in $GdBO_3$ microparticles at mesoscale by a high-gravity-assisted reactive precipitation-coupled calcination process. The high-gravity environment and tiny droplets generated by the high-gravity rotating packed bed (RPB) reactor lead to significant intensification of mass transfer and micromixing, which are beneficial for the homogeneous doping of Eu^{3+} in the host material during reactive precipitation in liquid solution. Under excitation at 395 nm, the emission spectra of the Eu^{3+}-doped phosphors exhibit a narrow-band red emission centered at 625 nm and the highest intensity was observed at $x = 0.2$. The RPB products show higher intensity than that of the control group even when the reaction time was shortened to 1/6. After calculation, the quenching in the sample most likely results from dipole−dipole interactions. The chromaticity coordinates for the RPB sample was measured as (0.598, 0.341) with a quantum yield of up to 78.11%, and the phosphors exhibit good thermal stability at 423 K. The phosphors were used as the luminescent materials for light-emitting diodes (LEDs), and the devices showed good performance. Our preliminary study illustrated that high-gravity-assisted approaches are promising for tuning the doping of rare-earth ions in microparticles at mesoscale toward efficient production of phosphors for LEDs.
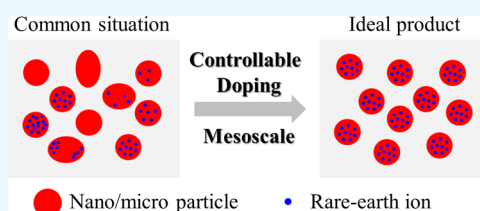
INTRODUCTION

The rare-earth-doped luminescent nanoparticles and microparticles have found many applications, and the rare-earth ions with emission in every color are revolutionizing applications from lighting devices to television displays.[1−5] For instance, light-emitting diodes (LEDs) based on the use of rare-earth-doped phosphors have been widely recognized as a green lighting source in favor of energy saving and environment protection.[6−9] In such a module, phosphors play crucial roles in determining the performance and quality of LEDs and the fast development of LED raises the demand of phosphors with uniform size distribution, high luminescence quantum efficiency, and high thermal stability.[10] Typically, the phosphors are made up of host materials and activators, while their optical properties are extremely sensitive to their structures in mesoscale.[11−14] The host materials include nitrogen/oxide,[15] aluminate,[16,17] silicate,[18] borate,[19] and fluorides.[20] The activators are usually rare-earth ions that can absorb high-energy photons and emit low-energy photons. The ideal product of rare-earth-doped phosphors should have a uniform particle size distribution and homogeneous doping ions in each particle, while in common situation the products are unevenly distributed either in size or component (Figure 1). Previous studies show that the general process of the rare-earth-doped particle formation involves the mixing of the reactants, precipitation of the precursors, and high-temperature
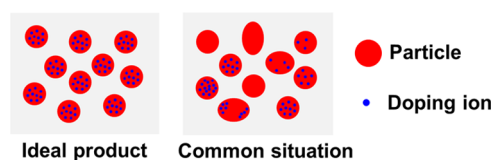

Figure 1. Schematic diagram of the ideal product and common situation of ion-doped inorganic nano/microparticles.

heat treatment of crystals.[21−23] The formation of primary particles in solution is usually the result of relative diffusion of solutes, and the main factor is the difference of diffusion concentration.[24] It is feasible to control and tune the characteristics of rare-earth-doped phosphors in lab-scale synthesis. However, it is very difficult to reproduce for scale-up due to the possible changes in reaction kinetics and thermodynamics.[25] To bridge the gap between the real products and ideal products of rare-earth-doped phosphors, tuning of the doping of rare-earth ions in nanoparticles and/or microparticles at mesoscale is therefore highly required.

In this work, we demonstrate the tuning of Eu^{3+} doping in $GdBO_3$ microphosphors by a high-gravity-assisted reactive

precipitation-coupled calcination process. A high-gravity rotating packed bed (RPB) reactor was used as the reactor for the reactive precipitation of precursor of $GdBO_3:Eu^{3+}$, followed by annealing to obtain microphosphors. The crystal structures, morphologies, and element distributions of $GdBO_3:Eu^{3+}$ microparticles were investigated by X-ray diffraction (XRD) and scanning electronic microscopy (SEM). The optical properties including luminescence spectra and luminescence quantum yields under excitation of near-ultraviolet (NUV) light were analyzed. The particles obtained by using conversial stirred tank reactors (STR) were adopted for comparison study. The LED devices fabricated by the $GdBO_3:Eu^{3+}$ microphosphors and NUV chips showed bright red emission, promising for applications in the next generation of semiconductor lighting.

■ RESULTS AND DISCUSSION

Two types of reactors including conversial STR and RPB were used for the mixing of the reactants for precipitation of the precursors during the preparation of $GdBO_3:Eu^{3+}$ micro-particles. The mixture of the reactants was allowed to react at room temperature in an STR or an RPB reactor for a certain time (in RPB for 10, 20, 30, 40, and 50 min, respectively, and in STR for 2 h). After that, the precipitations were annealed at 1200 °C for 4 h under air conditions to obtain particles with good crystallinity. The main chemical reaction in the solution can be described as follows
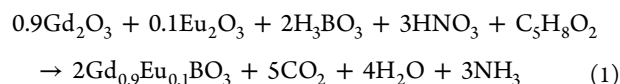
$$0.9Gd_2O_3 + 0.1Eu_2O_3 + 2H_3BO_3 + 3HNO_3 + C_5H_8O_2$$
$$\rightarrow 2Gd_{0.9}Eu_{0.1}BO_3 + 5CO_2 + 4H_2O + 3NH_3 \quad (1)$$

Figure 2a shows the XRD patterns of the products from the RPB route by reacting in the RPB reactor for various times
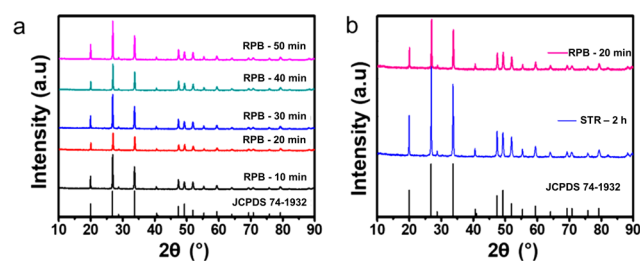

Figure 2. (a) XRD patterns of the products obtained via the RPB route by reacting in the RPB reactor for various times from 20 to 50 min and (b) XRD patterns of products obtained via the STR route by reacting in the STR for 2 h, followed by annealing at 1200 °C for 4 h under air conditions for all samples.

from 20 to 50 min. It was noted that the reaction time did not have significant effects on the crystal form of final products, which was attributed to the combination of the fillers and the strong centrifugal force in the RPB reactor. The liquid stream of the reactants is quickly cut into smaller liquid films and droplets,[26,27] allowing fast mixing of the reaction molecules and completion of the reaction in very short time.[28] Figure 2b shows the comparison of XRD patterns for samples RPB-20min and STR-2h. Although the reaction time in RPB is only 1/6 of that in STR, the two samples obtained from both RPB and STR routes exhibited similar crystal structures, which are in good agreement with the standard patterns of $GdBO_3$ crystal (JCPDS no. 74-1932). No significant impurity peaks were observed, indicating that the Eu^{3+} ions were completely

embedded into the $GdBO_3$ host lattices without significant effect on the crystal structures of the $GdBO_3$ lattices. The XRD data were further analyzed to calculate the unit cell parameters, which are shown in Tables S1 and S2. The cell parameters of the RPB-20min product are significantly closer to the unit cell parameters of the standard $GdBO_3$ ($a = b = 3.829$, $c = 8.89$) than that of the STR-2h product. These results were attributed to the enhanced mixing characteristics of the RPB reactor, which made the doping ions distribute more uniformly in the matrix lattices than those formed in conversial STR. The doping ions of Eu^{3+} uniformly replace the Gd^{3+} in the matrix lattice and the doping ratio is relatively low (10 atom %) so that the doping of Eu^{3+} ions has no significant effect on the formation of the host crystal form.

Figure 3 shows the SEM images and elemental distributions of Eu and Gd in the $GdBO_3:Eu^{3+}$ particles before and after
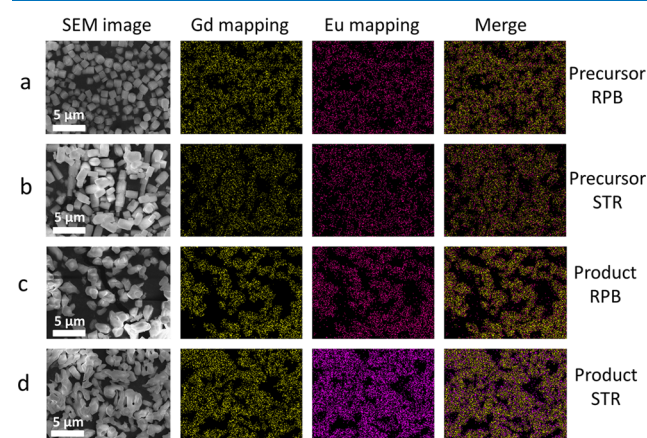

Figure 3. Typical SEM images of $GdBO_3:Eu^{3+}$ phosphors and the elemental mapping profiles of unannealed precursors synthesized by (a) RPB and (b) conversial STR and annealed products synthesized by (c) RPB route and (d) STR route. The reaction times in the RPB and STR were 2 h and 20 min, respectively.

annealing. Both samples exhibited a cylindrical shape before annealing, but the particles by reaction in RPB reactors showed a more regular shape and smaller size. The aspect ratio of the particles in the field of view is uniform and the surface is smooth. After annealing of the precursor, the samples obtained from RPB routes maintained their original particle sizes (about 2 μm) without significant agglomeration. The organic component disappears and the structure of cylinder changes. However, the samples prepared by the conversial STR route exhibited relative wide size distributions. The typical elemental mapping results, the merged images of Gd mapping and Eu mapping in particularly, indicated that the doping of Eu^{3+} ions in the $GdBO_3$ matrix was more uniformly dispersed in the samples of RPB (Figure 3a,c) than that in the samples of STR (Figure 3b,d). These results demonstrated that the use of the RPB reactor for mixing of the reactants and precipitation of the precursors was beneficial for tuning the doping of Eu^{3+} in $GdBO_3$ microparticles at mesoscale with a uniform distribution to form $GdBO_3$ microparticles with uniform size distribution and homogeneous doping ions.

In the excitation spectra of the samples shown in Figure 4a, several types of transition are observed. The peaks at 314 and 320 nm were assigned to $Gd^{3+} \rightarrow Eu^{3+}$, $^8S_{7/2} \rightarrow {}^6P_{5/2}$, $^8S_{7/2} \rightarrow {}^6P_{7/2}$ energy transfer. The $f \rightarrow f$ transition $^7F_0 \rightarrow {}^5L_6$ of Eu^{3+} was expressed as the peak around 395 nm, which was the most
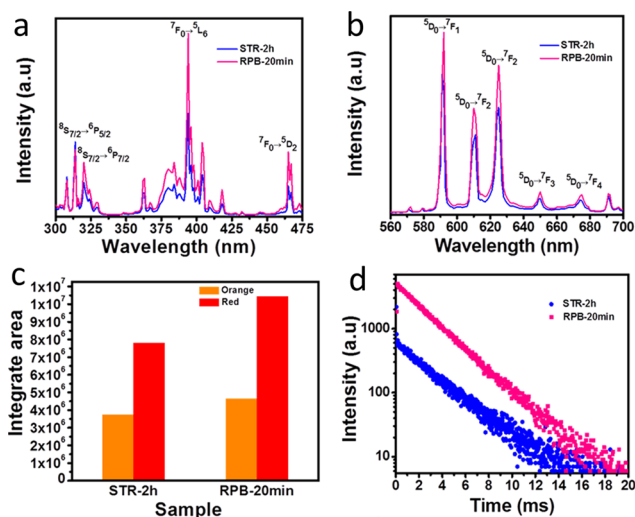
Figure 4. (a) Excitation spectra (λ_{em} = 625 nm) and (b) emission spectra (λ_{ex} = 395 nm) of GdBO$_3$:Eu^{3+} particles obtained by the STR route and RPB route. (c) Integrated area of red and orange emission intensity distribution in the emission spectra of the two samples. (d) Lifetime spectra of the two samples (λ_{ex} = 395 nm).

intensive in the field of vision. The emission spectra (Figure 4b) are composed of $^5D_0 \rightarrow {}^7F_J$ (J = 1−4) emission lines of Eu^{3+} and the peak at 592 nm is dominated by magnetic-dipole transition $^5D_0 \rightarrow {}^7F_1$ of Eu^{3+}, while the crystal field splits $^5D_0 \rightarrow {}^7F_2$ electric-dipole transition into two main lines at 610 and 625 nm. The emission lines located at 650 nm ($^5D_0 \rightarrow {}^7F_3$), 675 nm ($^5D_0 \rightarrow {}^7F_4$), and 691 nm ($^5D_0 \rightarrow {}^7F_4$) are also labeled in Figure 4b. It was noted that both spectra of the sample of RPB were significantly better than those of sample STR-2h. The ratio of red-to-orange emission intensities (R/O), $I(^5D_0-^7F_2)/I(^5D_0-^7F_1)$, is widely known as the asymmetric ratio.[29] Low site symmetry host materials exert a crystal field containing more odd components around rare-earth-doped ions and are more favorable for luminescence of the ions than those in their high symmetry counterparts. Therefore, on considering the sum of integral intensity of red emission peaks at 611 and 625 nm for $^5D_0-^7F_2$ and 590 nm for $^5D_0-^7F_1$, Figure 4c was presented, which indicated that the R/O ratio of RPB-20min (2.25) is higher than that of STR-2h (2.09). These results were attributed to the slight decrease in local symmetry around Eu^{3+} ions. In the decay spectra in Figure 4d, the red emission ($^5D_0 \rightarrow {}^7F_2$ transition) at 625 nm was determined by the following double-exponential formula[30,31]

$$I(t) = I_0 + A_1 \exp(-t/\tau_1) + A_2 \exp(-t/\tau_2) \quad (2)$$

In the formula, I and I_0 are the luminescence intensities at times t and 0 s and A_1 and A_2 are their fitting parameters. τ_1 and τ_2 indicate the corresponding decay times for the exponential components, especially τ_1 mainly determines the persisting performance of materials. Sample's defects might act as the channels of nonradiative relaxation, determining that the decay curves are double-exponential. The average lifetimes were calculate to be 2.97 ms (STR) and 2.56 ms (RPB). As demonstrated in a previous report,[23] an increase in the doping amount leads to a decrease in the decay time due to the cross-relaxation phenomenon between the Eu^{3+} ions. As per the results shown in Figure 3, the use of the RPB reactor increases the uniformity of doping. In other words, the use of the RPB reactor increased the effective dopant density of Eu^{3+} in the

particles. Therefore, the fluorescence lifetime of the RPB sample was shorter than that of STR.

The photoluminescence (PL) spectra of Gd$_{(1-x)}$BO$_3$/xEu^{3+} (x = 0.1, 0.15, 0.2, 0.25, 0.3, 0.35, and 0.4) phosphor with different Eu^{3+} doping concentrations under 395 nm excitation are shown in Figure 5. To determine which type of interaction mechanism dominates the energy transfer process among Eu^{3+} icons, we use the following equation[32]

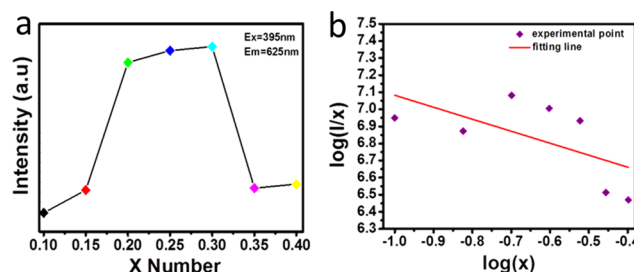$$\frac{I}{X} = K(1 + \beta^{\theta/3})^{-1} \quad (3)$$

Figure 5. (a) PL intensity of GdBO$_3$/xEu^{3+}(x = 0.1, 0.15, 0.2, 0.25, 0.3, 0.35, and 0.4) phosphor in 625 nm. (b) Plot of log(I/x) dependence of log(x) for the $^5D_0 \rightarrow {}^7F_2$ transition of Eu^{3+} ions in GdBO$_3$/xEu^{3+} phosphor under 395 nm excitation.

where I is the emission intensity, X refers to the activator concentration, and K and β are constants under the same excitation condition for the given host crystal. θ is a constant of multipolar interaction, and θ = 6, 8, 10 denotes electric d−d, d−q, q−q interactions, respectively. The relation between log(I/x) and log(x) is linear and the slop is −0.70, indicating that the nonradiative energy transfer mechanism among the Eu^{3+} ions in the host is the d−d interaction. These results further demonstrated that the performance of GdBO$_3$:Eu^{3+} phosphors was closely related to the mesoscale behavior and the uniform doping of Eu^{3+} in GdBO$_3$ microparticles.

It is known that the luminescent ions will reach the ground state via thermal quenching. They can go to the ground state when the excited state and the ground state energy curves cross at an energy that is thermally accessible from the relaxed excited state. The nonradiative rate, k$_{nr}$, can be expressed as[33]

$$k_{nr} = A \exp\left(-\frac{E_a}{kT}\right) \quad (4)$$

where A is a constant, k is Boltzmann's constant ($\approx 8.62 \times 10^{-5}$), and E_a is the activation energy for the thermal quenching process. The probability of nonradiative transition increasing with temperature leads to a decrease of emission intensity. Thermal quenching of the emission intensity of Eu^{3+} mainly accounts for the jumping of excited electrons into the charge-transfer state band with absorbing thermal energy, as schematically shown in Figure 6a, a condition in which the probability of nonradiative transition increases. Then, the emission intensity of Eu^{3+}-activated phosphor decreases. It can be seen from Figure 6b that the luminescence intensity of the GdBO$_3$:Eu^{3+} phosphors exhibited a slight increase as the temperature increases in the range of room temperature to 340 K and then remained steady in the range of 340−450 K, followed by a decrease over 450 K. This phenomenon was attributed to the following reason. The rise of temperature accelerates the molecular thermal motion to a certain extent to
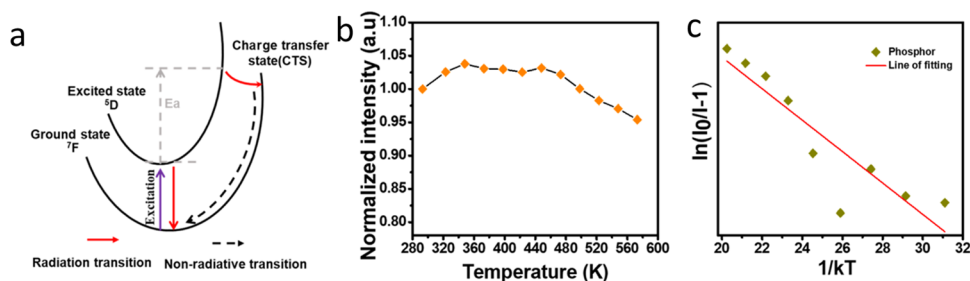
Figure 6. (a) Configurational coordinate showing the thermal quenching pathway for Eu^{3+} emission. (b) Normalized luminescent intensity of the $GdBO_3:Eu^{3+}$ phosphors at different temperatures. (c) Linear fitting curve of $\ln(I_0/I - 1)$ versus $1/kT$ for the phosphors.

Table 1. Luminescence Quantum Yields of Various Kinds of Red Phosphors and the Ratio of Luminescent Intensity at 423 K/303 K

phosphor	$Ca(GaO)_3(BO_3)_4:Ce^{3+}$	$Ba_3Lu_2B_6O_{15}:Ce^{3+},Tb^{3+}$	$Li_2SrSiO_4:Eu^{3+}$	$Na_2Gd(PO_4)(MoO_4):Eu^{3+}$	$GdBO_3:Eu^{3+}$
luminescence quantum yield (%)	49.5	51	62	37	78.1
luminescent intensity (423 K/303 K) (%)	50.5	54	80	63.3	≥98
refs	34	35	36	37	this work

promote the photon radiation transition. However, when the temperature reaches a certain value, the nonradiative transition dominates, resulting in a decrease in the luminous intensity. I_0 is used as a numerator in the formula because the fluorescence intensity is the strongest at ambient temperature by default. To ensure that $I_0/I - 1$ is a positive number, I_0 was defined as the intensity of emission at 348 K. As expressed by eq 4, a higher value of E_a means a lower nonradiative rate at a given temperature. In our experiments, the experimental data can be linearly fitted with a slope of −0.26 (Figure 6c), suggesting that the activation energy, E_a, was 0.26 eV. The small number of E_a further confirmed the good thermal stability of the $Gd_{(1-x)}BO_3/xEu^{3+}$ phosphor. By comparing with the phosphors reported,[34−37] it can be seen that the phosphor synthesized by our method excels in both quantum efficiency and thermal stability (Table 1), which was attributed to the following two reasons: First, the annealing treatment (1200 °C) is used in the preparation process, which makes the particle structure more tolerant to high temperatures. Second, since the radius of the B atom is smaller, the interaction force between the B atom and O atom is stronger and the bonding is more stable than that of other host materials, which leads to good thermal stability. Energy transfer among the dopants is the main reason for concentration quenching, which also greatly affects the quantum yield. The critical distance is roughly estimated by the following formula[34]

$$R_c = 2\left[\frac{3V}{4\pi X_c N}\right]^{1/3} \tag{5}$$

where R_C is the critical distance, V is the volume of the unite cell, X_c refers to the critical concentration, and N refers to the number of formula units per unit cell. For this system, the short distance between Eu^{3+} ions will lead to energy transfer between ions, increase the probability of nonradiative transitions, and weaken the fluorescence performance, similar to concentration quenching. When the distance between Eu^{3+} ions and Gd^{3+} ions is too long, the energy transfer between two ions is hindered and the energy utilization rate is reduced. The high-gravity RPB reactor can provide a homogeneous environment for the growth of particles, effectively control the distance

between rare-earth ions, successfully avoid the above disadvantages, and therefore improve the quantum yield.

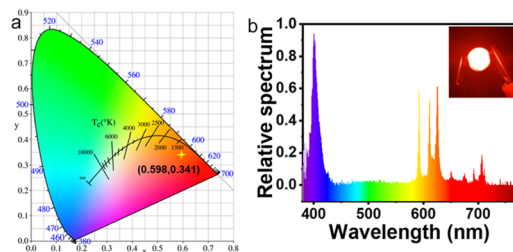Figure 7a shows the CIE coordinates of $GdBO_3:Eu^{3+}$ phosphors. The CIE coordinates of $GdBO_3:Eu^{3+}$ sample

Figure 7. (a) CIE picture of the $GdBO_3:Eu^{3+}$ phosphor. (b) Luminescence spectrum of the fabricated LED device with a 395 nm near-UV chip and $GdBO_3:Eu^{3+}$ phosphor (inset: photo of the lighted LED device).

were determined to be (0.598, 0.341), and the highest QY can reach 78.11%. Figure 7b shows the typical luminescence spectrum of a fabricated LED lamp with a 395 nm near-UV chip and $GdBO_3:Eu^{3+}$ phosphors, and the inset presents the photo of the respective device, in which significant red light is observed. These primary results demonstrated the potential of $GdBO_3:Eu^{3+}$ phosphors for NUV LEDs.

■ CONCLUSIONS

Inspired by the concept of "mesoscience",[38] we demonstrate a novel route toward efficient production of red phosphors for LEDs. By a high-gravity-assisted process intensification method to achieve uniform Eu^{3+} doping in $GdBO_3$ particles at mesoscale, the reaction time for the preparation of the precursor was reduced from 2 h in STR to 20 min in RPB. The product of red phosphors with luminescence quantum yield of up to 78.11% was obtained and makes one of the best red phosphors. The $GdBO_3:Eu^{3+}$ phosphors synthesized by high-gravity-assisted methods also show excellent thermal stability at 423 K, maintaining 98% of luminescent intensity at room temperature. The CIE chromaticity coordinates of the as-synthesized $GdBO_3:Eu^{3+}$ phosphor were determined to be (0.598, 0.341), and primary applications of these phosphors for

NUV LEDs were demonstrated. These studied illustrated that high-gravity-assisted approaches are promising for tuning the doping of rare-earth ions in microparticles at mesoscale toward efficient production of phosphors.

EXPERIMENTAL SECTION

Materials. Gadolinium oxide (Gd_2O_3, 99.9%), europium oxide (Eu_2O_3, 99.9%), boric acid (H_3BO_3, >99.5%), and acetylacetone ($C_5H_8O_2$, 99%) were bought from Aladdin Industrial Co. Ltd. (Shanghai, China). Nitric acid (HNO_3, 65%), urea (($NH_2)_2CO$, 99%), and ethanol (C_2H_5OH, 98%) were purchased from Beijing Chemical Works (Beijing, China), and poly(ethylene glycol)-1000 (PEG, 99%) was obtained from Bioruler Co. Ltd. All of the materials were used without further purification, unless otherwise stated. Deionized water, used for all processes, was prepared by the Hitech laboratory water purification system DW100 (Shanghai Hitech Instruments Co., Ltd.).

Preparation of $GdBO_3$:Eu^{3+} Phosphors. $GdBO_3$:Eu^{3+} phosphors (mole ratio of Eu/Gd = 1:9) were synthesized by a homogeneous precipitation-coupled calcination method. The stoichiometric amounts of Gd_2O_3 (3.26 g), Eu_2O_3 (0.352 g), H_3BO_3 (1.428 g), nitric acid (2.84 g), and PEG (4.42 g) were weighed, adding acetylacetone (4.32 mL) as the chelating agent, and mixed homogeneously with 100 mL of deionized water in a reactor. The reaction was allowed to be performed in conversional STR and RPB reactors, respectively. Afterward, 36 g of urea was added to the mixture and vigorously stirred at 90 °C for 1 h. The solid powder was separated by centrifugation and washed four times using deionized water and ethanol. The powder was dried at 80 °C for 5 h in an oven and then placed in a corundum crucible and covered up. After annealing in a furnace at 1200 °C for 5 h under an air atmosphere, the corundum crucible was naturally cooled down to indoor temperature. The phosphors synthesized by STR and RPB reactors are denoted STR-X and RPB-X, in which X represents the reaction time of the reactants in the respective reactors (10, 20, 30, 40, 50 min, and 2 h).

Fabrication of LED Devices. The near-UV chip and package glue were commercial products obtained from Ningbo Sunpu Led Co., Ltd. and Beijing KMT Technology Co., Ltd., respectively. Briefly, certain amounts of A glue (0.1 g), B glue (0.4 g), and $GdBO_3$:Eu^{3+} phosphors (0.2 g) were mixed homogeneously. The mixture was then dropped on the near-UV chips to cover the surface of the chips completely. Afterward, the LED devices were heated at 150 °C for 4 h and then cooled to the room temperature for testing.

Characterization. The crystal structures and phase purities were measured using an X-ray diffractometer (Ultima IV, Rigaku), with data collected at a scanning speed of 5° min^{-1} and a scanning angle from 10 to 80°. The photoluminescence (PL) spectra, photoluminescence excitation, fluorescence decay, quantum yield, and CIE spectra of samples were measured using a spectrophotometer (Edinburgh FS5) equipped with a 150 W continuous-wave Xeon lamp as the excitation source. The temperature-dependent PL spectra and LED test were measured by a fluorescence spectrometer (Yuanfangguangdian HAAS-2000 with temperature-increasing accessories TAP-02, Orient-KOJI Instrument Co. Ltd.). The particle morphology was characterized by scanning electron microscopy (JEOL JSM-7800F).

ASSOCIATED CONTENT

Ⓢ Supporting Information

The Supporting Information is available free of charge on the ACS Publications website at DOI: 10.1021/acsomega.9b01656.

XRD data of RPB-20 min and STR-2 h unburnt samples and calculated unit cell parameters of STR-2 h and RPB-20 min samples (PDF)

AUTHOR INFORMATION

Corresponding Authors
*E-mail: wangdan@mail.buct.edu.cn. Tel: +86-10-64449453 (D.W.).
*E-mail: puyuan@mail.buct.edu.cn. Tel: +86-10-64421905 (Y.P.).
ORCID ⓘ
Dan Wang: 0000-0002-3515-4590
Jie-Xin Wang: 0000-0003-0459-1621
Notes
The authors declare no competing financial interest.

REFERENCES

(1) Gai, S.; Li, C.; Yang, P.; Lin, J. Recent progress in rare earth micro/nanocrystals: soft chemical synthesis, luminescent properties, and biomedical applications. *Chem. Rev.* **2014**, *114*, 2343−2389.

(2) Van Loy, S.; Binnemans, K.; Gerven, T. V. Mechanochemical-assisted leaching of lamp phosphors: a green engineering approach for rare-earth recovery. *Engineering* **2018**, *4*, 398−405.

(3) Pu, Y.; Leng, J.; Wang, D.; Wang, J.-X.; Foster, N. R.; Chen, J.-F. Recent progress in the green synthesis of rare-earth doped upconversion nanophosphors for optical bioimaging from cells to animals. *Chin. J. Chem. Eng.* **2018**, *26*, 2206−2218.

(4) Pu, Y.; Leng, J.; Wang, D.; Wang, J.-X.; Foster, N. R.; Chen, J.-F. Process intensification for scalable synthesis of ytterbium and erbium co-doped sodium yttrium fluoride upconversion nanodispersions. *Powder Technol.* **2018**, *340*, 208−216.

(5) Wang, D.; Zhu, L.; Pu, Y.; Wang, J.-X.; Chen, J.-F.; Dai, L. Transferrin-coated magnetic upconversion nanoparticles for efficient photodynamic therapy with near-infrared irradiation and luminescence bioimaging. *Nanoscale* **2017**, *9*, 11214−11221.

(6) Savyasachi, A. J.; Caffrey, D. F.; Byrne, K.; Tobin, G.; D'Agostino, B.; Schmitt, W.; Gunnlaugsson, T. Self-assembled bright luminescent hierarchical materials from a tripodal benzoate antenna and heptadentate Eu(III) and Tb(III) cyclen complexes. *Front. Chem. Sci. Eng.* **2019**, *13*, 171−184.

(7) He, X.; Wang, Z.; Pu, Y.; Wan, D.; Tang, R.; Cui, S.; Wang, J.-X.; Chen, J.-F. High-gravity-assisted scalable synthesis of zirconia nanodispersion for light emitting diodes encapsulation with enhanced light extraction efficiency. *Chem. Eng. Sci.* **2019**, *195*, 1−10.

(8) Jiang, H.; Jia, Y.; Qu, T.; Pan, Y.; Yang, K.; Luo, H. Yellow persistent phosphor $Ba_{13.35}Al_{30.7}Si_{5.3}O_{70}$:$Eu^{2+}$,$Tm^{3+}$ from the energy regulation of rare-earth ions. *ACS Omega* **2019**, *4*, 6923−6930.

(9) Khan, S. A.; Zhang, H. Z.; Ji, W.; Hao, L.-Y.; Abadikhan, H.; Xu, X.; Khan, N. Z.; Agathopoulos, S. Single-phase white light-emitting $Ca_xBa_{(9−x)}Lu_2Si_6O_{24}$:$Eu^{2+}$/$Mn^{2+}$ phosphors. *ACS Omega* **2017**, *2*, 6270−6277.

(10) Tang, F.; Su, Z.; Ye, H.; Gao, W.; Pan, X.; Xu, S. Large negative-thermal-quenching effect in phonon-induced light emissions in Mn^{4+}-activated fluoride phosphor for warm-white light-emitting diodes. *ACS Omega* **2018**, *3*, 13704−13710.

(11) Wang, D.; Zhu, L.; Chen, J.-F.; Dai, L. Liquid marbles based on magnetic upconversion nanoparticles as magnetically and optically miniature reactors for photocatalysis and photodynamic therapy. *Angew. Chem., Int. Ed.* **2016**, *55*, 10795−10799.

(12) Leng, J.; Chen, J.; Wang, D.; Wang, J.-X.; Pu, Y.; Chen, J.-F. Scalable preparation of $Gd_2O_3:Yb^{3+}/Er^{3+}$ upconversion nanophosphors in a high-gravity rotating packed bed reactor for transparent upconversion luminescent films. *Ind. Eng. Chem. Res.* **2017**, *56*, 7977−7983.

(13) Nair, R. G.; Nigam, S.; Sudarsan, V.; Rao, R.; Vatsa, R. K.; Jain, V. K. Synthesis conditions on the nature of $GdBO_3$ phase formed. *ChemistrySelect* **2018**, *3*, 7496−7506.

(14) Shen, H.; Feng, S.; Wang, Y.; Gu, Y.; Zhou, J.; Yang, H.; Feng, G.; Li, L.; Wang, W.; Liu, X.; Xu, D. Synthesis and photoluminescence properties of $GdBO_3:Ln^{3+}$ (Ln = Eu, Tb) nanofibers by electrospinning. *J. Alloys Compd.* **2013**, *550*, 531−535.

(15) Ji, H.; Huang, Z.; Xia, Z.; Molokeev, M. S.; Atuchin, V. V.; Fang, M.; Huang, S. New yellow-emitting whitlockite-type structure $Sr_{1.75}Ca_{1.25}(PO_4)_2:Eu^{2+}$ phosphor for near-UV pumped white light-emitting devices. *Inorg. Chem.* **2014**, *53*, 5129−5135.

(16) Min, X.; Huang, Z.; Fang, M.; Liu, Y.-G.; Tang, C.; Wu, X. Energy transfer from Sm^{3+} to Eu^{3+} in red-emitting phosphor $LaMgAl_{11}O_{19}:Sm^{3+}$, Eu^{3+} for solar cells and near-ultraviolet white light-emitting diodes. *Inorg. Chem.* **2014**, *53*, 6060−6065.

(17) Zhang, N.; Tsai, Y.-T.; Fang, M.-H.; Ma, C.-G.; Lazarowska, A.; Mahlik, S.; Grinberg, M.; Chiang, C.-Y.; Zhou, W.; Lin, J. G.; Lee, J.-F.; Zheng, J. M.; Guo, C.; Liu, R.-S. Aluminate red phosphor in light-emitting diodes: theoretical calculations, charge varieties, and high-pressure luminescence analysis. *ACS Appl. Mater. Interfaces* **2017**, *9*, 23995−24004.

(18) Kim, J. S.; Kwon, O. H.; Jang, J. W.; Lee, S. H.; Han, S. J.; Lee, J. H.; Cho, Y. S. Long-term stable, low-temperature remote silicate phosphor thick films printed on a glass substrate. *ACS Comb. Sci.* **2015**, *17*, 234−238.

(19) Zhang, X.; Gong, M. Photoluminescence and energy transfer of Ce^{3+}, Tb^{3+}, and Eu^{3+} doped $KBaY(BO_3)_2$ as near-ultraviolet-excited color-tunable phosphors. *Ind. Eng. Chem. Res.* **2015**, *54*, 7632−7639.

(20) Zhou, Y.-Y.; Song, E.-H.; Deng, T.-T.; Zhang, Q.-Y. Waterproof narrow-band fluoride red phosphor $K_2TiF_6:Mn^{4+}$ via facile superhydrophobic surface modification. *ACS Appl. Mater. Interfaces* **2018**, *10*, 880−889.

(21) Grzyb, T.; Lis, S. Structural and spectroscopic properties of $LaOF:Eu^{3+}$ nanocrystals prepared by the sol-gel pechini method. *Inorg. Chem.* **2011**, *50*, 8112−8120.

(22) Yang, L.; Zhou, L.; Huang, Y.; Tang, Z. Controlled synthesis of different morphologies of $GdBO_3:Eu^{3+}$ crystals and shape-dependent luminescence properties. *Mater. Chem. Phys.* **2011**, *131*, 477−484.

(23) Szczeszak, A.; Grzyb, T.; Lis, S.; Wiglusz, R. J. Revision of structural properties of $GdBO_3$ nanopowders doped with Eu^{3+} ions through spectroscopic studies. *Dalton Trans.* **2012**, *41*, 5824−5831.

(24) Pu, Y.; Wang, J.-X.; Wang, D.; Foster, N. R.; Chen, J.-F. Subcritical water processing for nanopharmaceuticals. *Chem. Eng. Process.* **2019**, *140*, 36−42.

(25) Su, R.; Wang, D.; Liu, M.; Yan, J.; Wang, J.-X.; Zhan, Q.; Pu, Y.; Foster, N. R.; Chen, J.-F. Subgram-scale synthesis of biomass waste-derived fluorescent carbon dots in subcritical water for bioimaging, sensing, and solid-state patterning. *ACS Omega* **2018**, *3*, 13211−13218.

(26) Liu, H.; Hu, T.; Wang, D.; Shi, J.; Zhang, J.; Wang, J.-X.; Pu, Y.; Chen, J.-F. Preparation of fluorescent waterborne polyurethane nanodispersion by high-gravity miniemulsion polymerization for multifunctional applications. *Chem. Eng. Process.* **2019**, *136*, 36−43.

(27) He, X.; Tang, R.; Pu, Y.; Wang, J.-X.; Wang, Z.; Wang, D.; Chen, J.-F. High-gravity-hydrolysis approach to transparent nano-zirconia/silicone encapsulation materials of light emitting diodes devices for healthy lighting. *Nano Energy* **2019**, *62*, 1−10.

(28) Wang, Z.; Shi, J.; Wang, D.; Pu, Y.; Wang, J.-X.; Chen, J.-F. Metal-free catalytic oxidation of benzylic alcohols for benzaldehyde. *React. Chem. Eng.* **2019**, *4*, 507−515.

(29) Kang, F.; Zhang, Y.; Peng, M. Controlling the energy transfer via multi luminescent centers to achieve white light/tunable emission in a single-phased X_2-type $Y_2SiO_5:Eu^{3+},Bi^{3+}$ phosphor for ultraviolet converted LEDs. *Inorg. Chem.* **2015**, *54*, 1462−1473.

(30) Koparkar, K. A.; Bajaj, N. S.; Omanwar, S. K. Effect of partially replacement of Gd^{3+} ions on fluorescence properties of $YBO_3:Eu^{3+}$ phosphor synthesized via precipitation method. *Opt. Mater.* **2015**, *39*, 74−80.

(31) Zhang, X.; Zhou, L.; Pang, Q.; Gong, M. A broadband-excited and narrow-line $GdBO_3$: Ce^{3+}, Tb^{3+}, Eu^{3+} red phosphor with efficient Ce^{3+}-Tb^{3+}-Eu^{3+} energy transfer for NUV LEDs. *Opt. Mater.* **2014**, *36*, 1112−1118.

(32) Guo, H.; Sun, L.; Liang, J.; Li, B.; Huang, X. High-efficiency and thermal-stable Eu^{3+}-activated $Ca_3Y(AlO)_3(BO_3)_4$ red-emitting phosphors for near-UV-excited white LEDs. *J. Lumin.* **2019**, *205*, 115−121.

(33) Seraiche, M.; Guerbous, L.; Kechouane, M.; Potdevin, A.; Chadeyron, G.; Mahiou, R. VUV excited luminescence of $Gd_{0.9}Eu_{0.1}BO_3$ nanophosphor prepared by aqueous sol-gel method. *J. Lumin.* **2017**, *192*, 404−409.

(34) Li, B.; Huang, X.; Lin, J. Single-phased white-emitting $Ca_3Y(GaO)_3(BO_3)_4:Ce^{3+}$, Tb^{3+}, Sm^{3+} phosphors with high-efficiency: photoluminescence, energy transfer and application in near-UV-pumped white LEDs. *J. Lumin.* **2018**, *204*, 410−418.

(35) Huang, X.; Guo, H.; Sun, L.; Sakthivel, T.; Wu, Y. A high-efficiency, broadband-excited cyan-emitting $Ba_3Lu_2B_6O_{15}:Ce^{3+},Tb^{3+}$ phosphor for near-UV-pumped white light-emitting diodes. *J. Alloys Compd.* **2019**, *787*, 865−871.

(36) Nasir, S. S. B.; Tanaka, A.; Yoshiara, S.; Kato, A. Luminescence properties of $Li_2SrSiO_4:Eu^{2+}$ silicate yellow phosphors with high thermal stability for high-power efficiency white LED application. *J. Lumin.* **2019**, *207*, 22−28.

(37) Huang, X.; Guo, H.; Li, B. Eu^{3+}-activated $Na_2Gd(PO_4)$-(MoO_4): a novel high-brightness red-emitting phosphor with high color purity and quantum efficiency for white light-emitting diodes. *J. Alloys Compd.* **2017**, *720*, 29−38.

(38) Li, J. Exploring the logic and landscape of the knowledge system: multilevel structures, each multiscaled with complexity at the mesoscale. *Engineering* **2016**, *2*, 276−285.